Crane Spreader Pose Estimation from a Single View

Maria Pateraki[1,2,3][a], Panagiotis Sapoutzoglou[1,2][b] and Manolis Lourakis[3][c]

[1]*School of Rural Surveying and Geoinformatics Engineering, National Technical University of Athens, Greece*

[2]*Institute of Communication and Computer Systems, National Technical University of Athens, Greece*

[3]*Institute of Computer Science, Foundation for Research and Technology – Hellas, Greece*

Keywords: Spreader, 6D Pose, Estimation, Single View.

Abstract: This paper presents a methodology for inferring the full 6D pose of a container crane spreader from a single image and reports on its application to real-world imagery. A learning-based approach is adopted that starts by constructing a photorealistically textured 3D model of the spreader. This model is then employed to generate a set of synthetic images that are used to train a state-of-the-art object detection method. Online operation establishes image-model correspondences, which are used to infer the spreader's 6D pose. The performance of the approach is quantitatively evaluated through extensive experiments conducted with real images.

1 INTRODUCTION

Standard size shipping containers transfer easily between transport modes and are the single most important system for the movement of cargo worldwide (van Ham et al., 2012). Container handling is fully mechanized and relies predominately on cranes equipped with spreaders, i.e. lifting devices which mechanically lock on to containers. Digitization is currently a trend that is gaining momentum in container logistics, aiming to make related processes more automated, efficient and traceable. Under these premises, we are interested in monitoring the 6D pose of a container crane spreader during container loading and unloading operations. Knowledge of the spreader's pose can provide input for various uses, e.g. improve the crane operator's situational awareness and hence the safety of port workers (Lourakis and Pateraki, 2022a), ensure that the operator's driving commands are within the crane's safe operating envelope or perform anti-sway crane control to eliminate undesirable oscillations (Ngo and Hong, 2012).

Numerous visual tracking methods have been developed and those focusing on 3D tracking (Lepetit and Fua, 2005; Marchand et al., 2016) can in principle facilitate the need for constant monitoring of a spreader's pose. However, a serious practical shortcoming of such approaches is that they often are not concerned with bootstrapping but rather assume that tracking is initialized by external, typically manual means. In addition to bootstrapping, periodic initialization is also necessary for recovering from tracking failures. To address such issues, this work employs recent results from the object detection and localization literature to deal with spreader 6D pose estimation from a single image. To the best of our knowledge, our results are the first ones reported dealing with this particular problem.

The main contributions of our work are: a) the application of vision techniques to a new domain, b) a procedure for generating a training dataset based on systematically rendering a photorealistic object model from different camera viewpoints, and c) a detailed experimental evaluation of a state-of-the-art object detection and localization method (Hodaň et al., 2020a) in a real-world setting. The remainder of the paper is organized as follows. An overview of object detection and localization approaches is provided in Section 2. The adopted methodology is presented in Section 3 and evaluated with the dataset described in Section 4. The results of the evaluation are presented in Section 5 and the paper concludes in Section 6.

2 PREVIOUS WORK

Object detection and localization are widely studied topics in the computer vision community with most

[a] https://orcid.org/0000-0002-8943-4598
[b] https://orcid.org/0000-0001-9885-3981
[c] https://orcid.org/0000-0003-4596-5773

Pateraki, M., Sapoutzoglou, P. and Lourakis, M.
Crane Spreader Pose Estimation from a Single View.
DOI: 10.5220/0011788800003417
In *Proceedings of the 18th International Joint Conference on Computer Vision, Imaging and Computer Graphics Theory and Applications (VISIGRAPP 2023) - Volume 5: VISAPP*, pages 796-805
ISBN: 978-989-758-634-7; ISSN: 2184-4321

recent reviews emphasizing the application of deep learning techniques to both these problems, e.g. (Kim and Hwang, 2021; He et al., 2021b; Sahin and Kim, 2018; Rahman et al., 2019). The recovery of 6D pose from a single 2D image is an ill-posed problem due to the lack of depth. To account for the absence of depth, researchers rely on exploiting multiple views (Labbe et al., 2020; Sun et al., 2022), assume geometric priors (Hu et al., 2022), or use 3D information from different sensors (He et al., 2021b).

In contrast to traditional methods exploiting handcrafted features and optimizing classic pipelines, deep learning methods led to significant improvements in 6D object pose estimation in late years (Jiang et al., 2022). However, a major shortcoming is that these approaches are extremely data driven and, contrary to 2D vision tasks such as classification, object detection and segmentation, the acquisition of 6D object pose annotations is much more labor intensive and time consuming (Hodan et al., 2017; Wang et al., 2020). To mitigate the lack of real annotations, synthetic images can be generated via 6D pose sampling and graphics rendering of a CAD object model. Still, there remains the concern of this approach performing poorly when applied to real world images, due to the domain gap between real and synthetic data (Wang et al., 2020).

Most recent works in object 6D pose estimation achieve high scores in recall accuracy on benchmark datasets (He et al., 2021a). However, transferring this performance to real environments is challenging. Uncontrolled imaging conditions such as dynamic background, changing illumination, occlusion, etc, that are often encountered in outdoor environments, further aggravate the problem. In the particular case of a spreader, additional challenges are the large changes in its appearance and apparent size, cast shadows and motion blur due to rapid motions and crane vibrations.

Contemporary pose estimation methods based on the use of deep learning with RGB images have, to a certain extent, succeeded in effectively handling objects with weak texture and symmetries. In the context of the 2020 BOP challenge (Hodaň et al., 2020b), several recent approaches were compared against benchmark datasets that feature objects with weak texture and symmetries, such as T-LESS (Hodan et al., 2017), LM-O (Brachmann et al., 2014) and ITODD (Drost et al., 2017). The CosyPose (Labbe et al., 2020) and EPOS (Hodaň et al., 2020a) methods are reported to require 0.5–2 sec processing time per image, while others exceed 1 min and are therefore less suitable for near real-time applications. Apart from being computationally efficient, EPOS effectively manages global and partial object symmetries, therefore it was selected as the basis of spreader pose estimation in this work.

3 METHODOLOGY

3.1 Overview

Training a neural model for the detection and 6D pose estimation of a spreader requires the collection of a large number of training images that depict the spreader from various vantage points. Owing to the spreader's large physical dimensions and the practical difficulties of thoroughly imaging it under controlled conditions for recovering the ground truth poses, amassing an adequate training dataset is far from being a trivial task. To overcome this, it was decided to employ synthetic images for training, hence a photorealistic textured model of the spreader was constructed first. Then, the training dataset was generated by systematically rendering images of the textured spreader model from different camera viewpoints which densely sample the 6D pose space. Equipped with a trained model, online inferencing with EPOS permits the recovery of the 6D spreader pose. More details are provided in the subsections that follow.

3.2 Object Pose Estimation

The EPOS method (Hodaň et al., 2020a) relies primarily on RGB images while additional depth information may be exploited to improve the accuracy of the required rendering of object models. Objects are represented via sets of compact surface regions called fragments, which are used to handle symmetries by predicting multiple potential 2D-3D correspondences at each pixel. EPOS establishes 2D-3D correspondences by linking pixels with predicted 3D locations and then a Perspective-n-Point (PnP) algorithm embedded in a RANSAC (Fischler and Bolles, 1981) framework is used to estimate the 6D pose.

Initially, a regressor associates each of the surface fragments of the object to predict the corresponding 3D location expressed in 3D fragment coordinates. Then, a single deep convolutional neural network (CNN) with a DeepLabv3+ (Chen et al., 2018) encoder-decoder is adopted to densely predict a) the probability of each object's presence, b) the probability of the fragments given the object's presence, and c) the precise 3D location on each fragment in 3D fragment coordinates. For training the network, a per-pixel annotation in the form of an object label, a fragment label, and 3D fragment coordinates are provided. Hypotheses are next formed by a locally optimized RANSAC variant (Barath and Matas, 2018) and pose is estimated by the P3P solver of (Kneip et al., 2011). Finally, pose is refined from all inliers using the EPnP solver (Lepetit et al., 2009) followed by non-linear minimization of the reprojection error.

3.3 Pose Error Metrics

To assess the error pertaining to the pose estimated for an image frame, different metrics are employed. The first set of metrics quantifies the absolute angular and positional errors with respect to the ground truth. More specifically, given the true camera rotation $\mathbf{R}_g$ and translation $\mathbf{t}_g$, the error for an estimated rotation $\mathbf{R}_e$ is the angle of rotation about a unit vector that transfers $\mathbf{R}_e$ to $\mathbf{R}_g$, computed as $\arccos((\mathrm{trace}(\mathbf{R}_g\mathbf{R}_e^T)-1)/2)$ (Huynh, 2009). The absolute error for an estimated translation $\mathbf{t}_e$ is the magnitude of the difference of the translation parts, i.e. $||\mathbf{t}_g - \mathbf{t}_e||$ with the vertical bars denoting the vector norm. The second set of metrics are the relative angular and positional errors as employed by (Lepetit et al., 2009). These are respectively calculated as $||\mathbf{q}_g - \mathbf{q}_e||/||\mathbf{q}_e||$, where $\mathbf{q}_g$ and $\mathbf{q}_e$ are the unit quaternions corresponding to the rotation matrices, while the relative error of an estimate $\mathbf{t}_e$ is given by $||\mathbf{t}_g - \mathbf{t}_e||/||\mathbf{t}_e||$.

Further to these metrics, we also used the average distance for distinguishable (ADD) objects (Hinterstoisser et al., 2012), which quantifies the average misalignment between the model's vertices in the true and estimated pose by calculating the average distance between corresponding mesh model vertices transformed by the ground truth and the estimated pose. More concretely, for a mesh model with N vertices $\mathbf{x}_i$, the ADD alignment error is given by

$$E = \frac{1}{N}\sum_{i=1}^{N} ||(\mathbf{R}_g\mathbf{x}_i + \mathbf{t}_g) - (\mathbf{R}_e\mathbf{x}_i + \mathbf{t}_e)||, \qquad (1)$$

where $\{\mathbf{R}_g,\ \mathbf{t}_g\}$ is again the true pose and $\{\mathbf{R}_e,\ \mathbf{t}_e\}$ the estimated one. The first and second set of metrics consider the angular and positional errors separately, whereas the ADD indirectly accounts for both pose components simultaneously.

3.4 Object Model Texturing

Application of EPOS requires high fidelity textured 3D models of the objects of interest to be available. In the case of the crane spreader, a textureless mesh model was initially designed with the aid of CAD software, using actual physical dimensions obtained from engineering diagrams. The opening of the telescopic beams of the spreader model was chosen to match that of a 40 ft container. The model has medium level detail and consists of 724 faces and 332 vertices. More detailed models were avoided as they do not noticeably improve the accuracy of pose estimation, while incurring a larger computational cost to be rendered. To construct a photorealistic textured model, a set of images were collected with a handheld commodity camera from different viewpoints around the spreader and combined together with its CAD mesh model for texture mapping.

Based on freely available software tools, two different texturing approaches were tested. The first employed the MeshLab[1] open source software and its integrated workflow for texture mapping. The standard approach for texturing a model's polygons is to extract the texture from the image whose camera optical axis is as close to being parallel to a certain face normal as possible. Although the camera position of the images was correctly estimated from manual raster alignment in MeshLab, in some cases the texture was taken from images for which the angle between the camera axis and the surface normal was not the smallest, resulting in perspective distortions. Further investigation into this issue revealed that MeshLab generally assumes that the input geometric models consist of dense meshes, for which such perspective errors are barely visible. However, this texture mapping workflow is less suited to CAD models with sizeable triangular faces as is the case with the spreader model.

The second approach was based on Blender[2], which has certain provisions for automatically projecting images to meshes, though it assumes simple geometric shapes. For the spreader, a manual texture mapping process was followed, summarized as follows. First, the model's origin and axes were transformed to conform to the input conventions of the training data later used by EPOS for object pose inference. Then, a UV texture map was generated automatically in Blender unfolding the model faces based on edges characterized as "sharp", i.e. edges formed by two adjacent faces with an angle between their normals exceeding a threshold value. For certain faces that Blender erroneously marked as being non-coplanar, despite their normals exhibiting negligible differences, a postprocessing step was carried out on the mesh model. Specifically, a plane was fitted to selected points to assess whether large errors were present and then the mesh was re-triangulated generating coplanar faces. For a few self-occluded parts of the spreader that did not appear in any image, texture was sampled from nearby image areas to

[1]https://www.meshlab.net
[2]https://www.blender.org

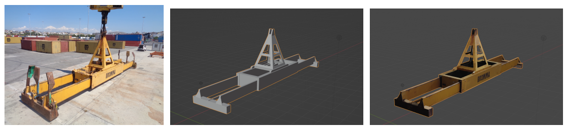

Figure 1: The crane spreader (left), and renderings of its mesh (middle) and final textured models (right). For simplicity, the three moving gather guides at each end beam of the spreader have not been modeled.

fill the remaining empty regions. Sample views of the mesh model and the final textured model are in Fig. 1.

3.5 Image Rendering

For rendering the training dataset (see Sec. 3.6), a custom renderer based on OpenGL's shader pipeline was developed. This renderer encompasses different shaders to perform wireframe, textured and depth rendering. Specifically, for depth map generation, depth was computed using a depth shader that transforms the vertex coordinates of the model to the viewspace of the camera. The depth value was then obtained by negating the z component of the resulting points.

In addition to the aforementioned rendering procedure, an algorithm for hidden lines removal based on z-buffering was developed that proved very useful for the visual assessment of the estimated poses on the test sequences (see Sec. 5). Hidden lines removal is closely associated with the wireframe display mode and is used to suppress the rendering of edges that are occluded from a certain camera perspective. Additionally, it discards nominal edges (i.e. edges/lines that separate faces which are coplanar and thus belong to the same plane). To discard edges occluded from the camera viewpoint, the algorithm uses the depth buffer to store the depth of each fragment of the model when rendered and performs a depth test with a depth mask of the scene rendered with lines. Furthermore, the nominal edges are excluded by computing the normals cross product for every pair of adjacent faces. If the cross product is close to zero, the edge is discarded as being nominal (e.g. a subdivision of a quad face into two triangles).

3.6 Training Dataset

Training data were generated by systematically rendering the textured spreader model against a black background from different camera viewpoints, thus densely sampling different 6D poses of the spreader. With the spreader model placed at the center of a half sphere and the use of spherical coordinates ϕ and θ, different images were rendered at camera positions around hemispheres of radial distances ranging from 10 to 30 meters with a step of 5 meters (see Fig. 2).

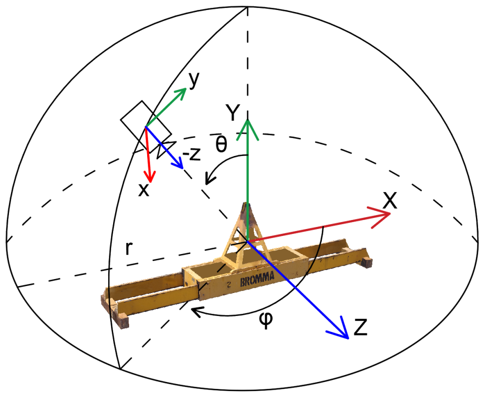

Figure 2: The spherical coordinate system employed in sampling the 6D space of spreader poses for training.

The azimuthal angle ϕ was set in the range of 0-360 degrees whereas the polar angle θ in the range of 0-90 degrees. For both angles, the step interval for rendering different viewpoints was set to 5 degrees. Values of θ exceeding 90 degrees were not considered as bottom views of the spreader are not encountered in reality and hence were excluded from the training dataset. A total of 6840 images were generated. Indicative thumbnails of rendered views at a distance of 10 m from the spreader's centroid are shown in Fig. 3.

The rendered images used for training were 720×540 pixels as that was the largest size that could be accommodated in the memory available on the particular GPU card used in the experiments (i.e. NVIDIA GeForce RTX 3060). 75% of the rendered dataset, i.e. 5130 images, were randomly selected for training, whereas the remaining 25% (i.e. 1710 images) were used for validation. Hyperparameters were tuned based on a number of experiments optimizing in parallel the training loss. The base learning rate was set to 3×10^{-5} and a polynomial decay learning rate schedule was used with power equal to 0.7, while the number of training steps was 2×10^{6}. Results on the training loss are shown in Fig. 4. The total loss and the training loss for visible object classification are shown in the top left and top right, while in the bottom left and bottom right are the training loss for visible fragments and the fragment localization loss. For the latter, regression is used for estimating the 3D coordinates of the fragments. In all four cases, the total loss has gradually reduced and finally stabilized.

Figure 5 shows sample qualitative results on the validation data regarding the predicted poses. The error metrics illustrated in Fig. 6 depict the distribution of the absolute angular and positional errors. In addition, the distributions of the relative angular and positional errors, as well as the ADD errors are also shown. To account for rotational symmetry in

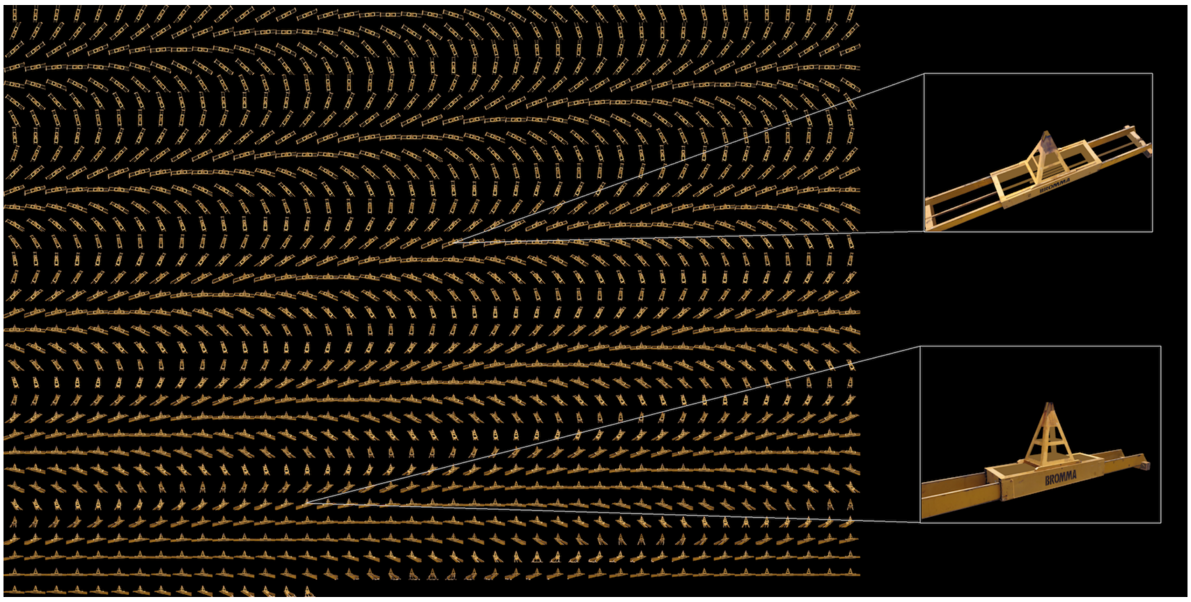

Figure 3: Sample rendered images of the spreader model around a hemisphere of radius of 10 m, with an azimuthal angle ϕ range of $[0^\circ - 360^\circ]$ and polar angle θ range of $[0^\circ - 90^\circ]$ with an increment of 5°.

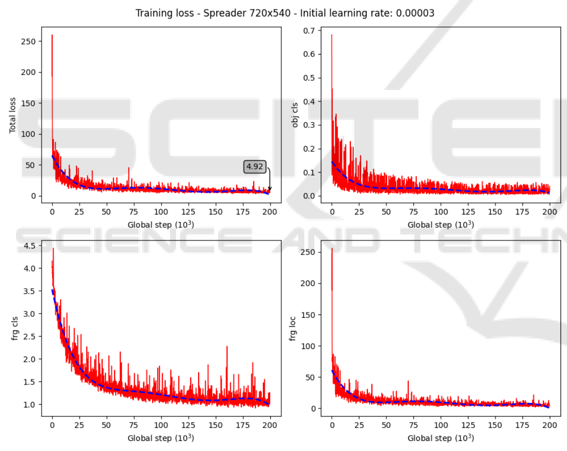

Figure 4: Total loss and number of steps (top left), training loss for visible object classification (top right), training loss for visible fragments (bottom left) and fragment localization loss (bottom right).

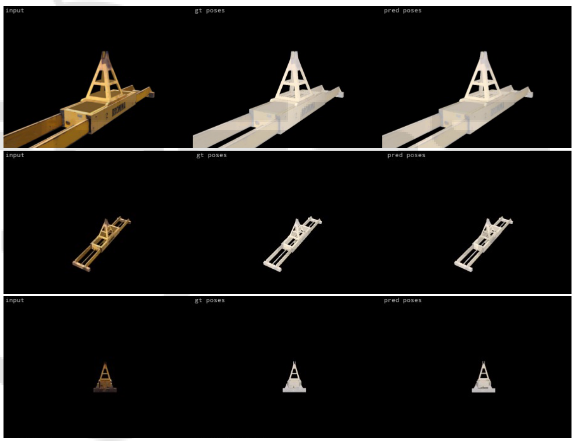

Figure 5: Example image results on validation data. Input image (left), ground truth pose (middle), regressed/predicted pose (right).

the vertical (i.e., z) axis of the spreader, the errors for both the estimated and the flipped pose (i.e., rotated by π around the z-axis) were considered and the pose yielding the smallest of the two was used in the calculation of the final errors. The absolute angular errors are in general below 1° and the absolute positional errors below 0.1 m. The relative angular and positional errors are below 0.01 in both cases, whereas the ADD error is in most cases below 0.04 m.

3.7 Background Removal

Preliminary tests with real images indicated that background clutter present in them often gave rise to erroneous poses, thus it was decided to perform a 2D segmentation of the spreader before inference. In order to eliminate the background, a model was trained to automatically detect the region corresponding to the spreader's image and then use it as a 2D mask for performing pose inference.

The dataset for training the mask detector comprised of a number of annotated frames for training and validation. A total of 224 frames (188 training

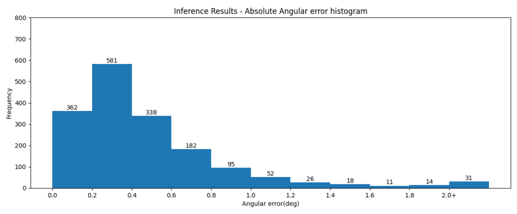

(a)

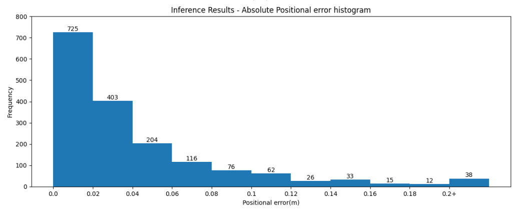

(b)

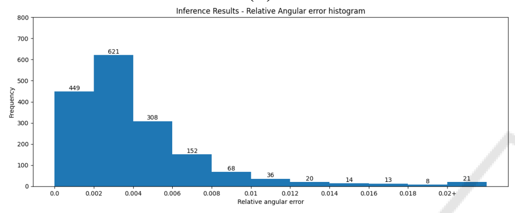

(c)

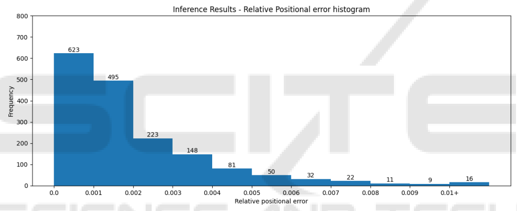

(d)

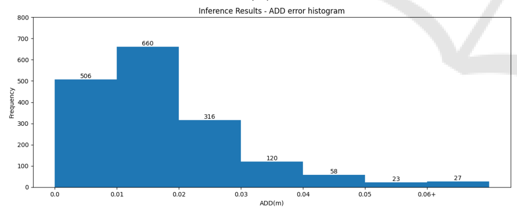

(e)

Figure 6: Results on validation data (1710 images). (a) absolute angular errors, (b) absolute positional errors, (c) relative angular errors, (d) relative positional errors and (e) mean misalignment errors (ADD).

and 36 validation) with sufficient diversity in spreader poses, and originating from five different video sequences acquired in the port environment were manually annotated using the VGG Image Annotator[3]. In order for the dataset to fit in the available GPU memory, its image frames were resampled to 1024×768 while maintaining their original aspect ratio.

Initially, we experimented with the Tensorflow-based implementation of the Mask R-CNN algo-

[3]https://www.robots.ox.ac.uk/~vgg/software/via/

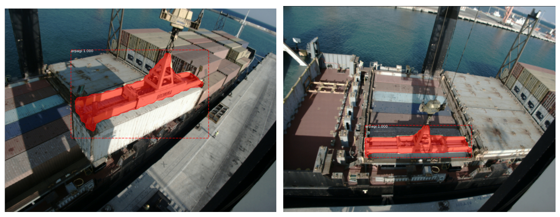

Figure 7: Results on 2D segmentation with the Mask R-CNN algorithm. The inaccuracies of the detected mask boundaries are clearly visible in the left image.

rithm (He et al., 2017). The inference results were mostly accurate but in certain frames the spreader was not segmented correctly, with the segmentation masks also exhibiting a wave effect at their boundaries, as shown in Fig. 7. In an effort to alleviate these problems, we used the Detectron2 library (Wu et al., 2019), which in addition attains shorter training times due to the PyTorch-based implementation of Mask R-CNN.

4 REAL IMAGES AND GROUND TRUTH POSES

The images we employed for evaluation originate from our publicly available dataset which depicts a moving crane spreader while unloading a container cargo vessel (Lourakis and Pateraki, 2022b). The dataset consists of several image sequences containing segments with the spreader being vacant and carrying a container. All image sequences were acquired from a viewpoint similar to that of the crane operator using a camera installed next to the operator's cabin at a height of approximately 20 meters above the quay. Owing to this setup, the camera moves with the crane, giving rise to a non-stationary image background. This further induces large variability in illumination within each image sequence and across the image sequences comprising the dataset, as the sequences were captured outdoors at different times of the day.

For every image frame, the dataset includes the corresponding ground truth pose of the spreader. Acquiring ground truth poses for real world sequences entails certain manual effort and is a rather arduous task. Before proceeding to the presentation of results, it is important to describe how were the ground truth poses for the dataset obtained since the procedure adopted impacts their accuracy.

Initially, the following options were considered for the spreader and were both deemed inapplicable. Non-visual sensors, e.g. RTK GNSS receivers (Lourakis et al., 2020) could not be deployed due to installation limitations and the fact that their measurements would be adversely affected by interference caused by the crane's metallic structure. Another choice would be the installation of visual fiducial markers (Garrido-Jurado et al., 2014) on the spreader, however this would affect its appearance and consequently potentially interfere with the pose estimation process. Alternatively, ground truth poses were obtained with the following semi-automatic procedure. The spreader's pose in a certain image frame was estimated by first delineating in that image a few characteristic line segments whose pre-images in the spreader's mesh model were easily identifiable and then using them to estimate a preliminary spreader pose with a Perspective-n-Line (PnL) solver (Wang et al., 2019) embedded in RANSAC (Fischler and Bolles, 1981) for safeguarding against outliers. Finally, the preliminary pose estimate was refined with non-linear least squares by minimizing the re-projection error between the actual image line segments and their predicted locations with Levenberg-Marquardt (Lourakis, 2004).

To obtain the spreader's poses for an entire video sequence, the pose in the first frame of the sequence was estimated with the procedure outlined in the previous paragraph, using a few model-to-image correspondences that were specified manually. This first-frame pose was used to initialize our tracker from (Lourakis and Pateraki, 2021) and the spreader was tracked until the model of the spreader rendered on images with the estimated pose began to visually deviate from its true image. At the underlying frame, the pose was again estimated interactively with PnL and Levenberg-Marquardt refinement, the tracker was re-initialized with it and the process was repeated as many times as necessary for the remaining frames. In this manner, the pose was estimated interactively at certain intermediate keyframes (typically up to a handful for each sequence) and then propagated by frame-to-frame tracking between them. This procedure enabled the collection of ground truth poses with limited manual intervention in a reasonable amount of time. The trade-off is that the data obtained are actually pseudo ground truth.

5 EVALUATION RESULTS

This section provides quantitative experimental results regarding the accuracy of the single-view pose estimator using images captured in a real port environment as discussed in Section 4. In addition to pose accuracy, computational performance on two low-cost GPU models is also assessed. The employed images have a resolution of 1928×1448 pixels. Prior to further processing, images were undistorted and subsampled to a lower resolution, maintaining their aspect ratio. In the reported experiments, eight image sequences were used, each being several hundred frames long and with a total number of around 7000 image frames.

The background of each input image was segmented out as described in Section 3.7. After segmentation, the 2D mask of the foreground (i.e., presumably the spreader) was scaled to match the image size of the inference images used in the test sequences (1024×768 and 720×570). Additionally, a rigid transformation was applied to compensate for the different axes and coordinate origin conventions employed in EPOS. Specifically, EPOS requires the model's origin to be on the center of its 3D bounding box, and the z axis to point upward. The model was trained with the spreader being centered in images, whereas in the test image sequences the spreader may appear in different locations near the periphery of an image. Therefore, before running the estimator, each masked image was warped to a new one by applying a homography transforming the center of the spreader's bounding box to the image principal point. This homography has the effect of rotating the ray corresponding to the bounding box center so as to make it coincide with the camera principal axis. The underlying rotation matrix was also used to transform the ground truth poses so that the spreader is centered in the new images. The final pre-processing step regards adjusting the camera intrinsic parameters according to the image size used for the inference, while maintaining a constant aspect ratio. The transformed ground truth poses used in the inference were computed as

$$[\mathbf{R} \mid \mathbf{t}]_c = \mathbf{R}_h \cdot [\mathbf{R} \mid \mathbf{t}]_{\mathrm{GT}} \cdot \begin{bmatrix} \mathbf{R}_s & \mathbf{O} \\ \mathbf{0} & 1 \end{bmatrix} \cdot \begin{bmatrix} \mathbf{I} & \mathbf{t}_{\mathrm{tr}} \\ \mathbf{0} & 1 \end{bmatrix}, \quad (2)$$

where $[\mathbf{R} \mid \mathbf{t}]_c$ is the transformed ground truth pose (according to EPOS conventions), $\mathbf{R}_h$ is the rotation matrix centering the spreader, $\mathbf{R}_s$ is the rotation for the y-z axis swap and $\mathbf{t}_{\mathrm{tr}}$ is the transformation to set the origin to the spreader's 3D bounding box.

The trained model for pose estimation was initially assessed on two sequences with different image resolutions, namely 1024×768 and 720×540 pixels, to investigate the relation of image resolution with the 6D pose errors and the inference times. The experiments confirmed that the inference time was reduced using images with resolution 720×540 pixels without significantly increasing the pose error metrics. The main reason is that the images used for training were 720×540 pixels in size. Yet, in both cases accuracy dropped for distant views of the spreader as in such

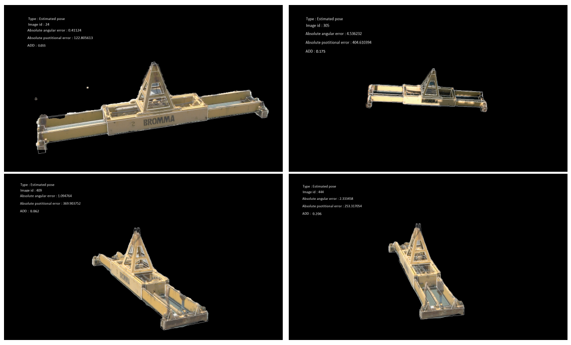
Figure 8: Indicative results from the test sequences with the predicted pose and the visible rendered model edges superimposed in white *(best viewed zoomed in)*.

situations the spreader is imaged in a small number of pixels.

Indicative image results are shown in Fig. 8, where the ADD, absolute angular and absolute translational errors are reported. For a qualitative visual assessment, the visible wireframe lines of the model are rendered superimposed on the input images. A correctly estimated pose should give rise to an overlaid model that aligns well with the contours and surfaces of the actual spreader in an image. Figure 9 illustrates the mean ADD error obtained for each image sequence of the dataset, whereas Fig. 10 depicts the distribution of ADD errors for the two image sequences comprised of the largest number of frames. For the most part, the mean misalignment error is less than 0.7 m and in the majority of the sequences below 0.3 m. Furthermore, the distribution of the errors in two indicative sequences with approximately 1300 frames each indicates that errors tend to be less than 0.2 m. We note at this point that the literature often considers a pose to be correct if its ADD is below a threshold chosen as the 10% of the object diameter (Hinterstoisser et al., 2012), which for the 12.44 m of the spreader equals 1.244 m. Table 1 summarizes for each sequence the minimum, mean and maximum figures for the ADD, absolute angular and positional error.

The mean absolute angular errors are in general below 5° except for one sequence (i.e., 095324), in which the mean absolute angular error increases to around 8°. It has been further observed that errors tend to be about $2^\circ - 3^\circ$ and for distant views the errors may increase up to $5^\circ - 6^\circ$. For the same sequences, the mean absolute positional errors are about 0.5 m − 0.6 m and for far away views less than 3.5 m. It is to be noted that the larger errors in one sequence are partially attributed to erroneous segmentation in cases of nearby objects having similar color distributions with these of the spreader and partly to inaccurate ground truth poses. To mitigate the effect of the latter, it was decided to exclude images yielding highly erroneous poses from further consideration in the computation of the error statistics. Thus, 90% of the frames with smaller ADD errors were retained, discarding the remaining 10%. The choice of the ADD instead of the absolute angular or positional error for selecting these frames is justified by the fact that we are mostly interested in the misalignment of the spreader at the estimated pose with respect to its ground truth configuration rather in the magnitude of the angular or positional error. An additional argument in favor of a surface alignment metric is that for elongated objects like the spreader, a small deviation in rotation can still result in a substantial misalignment of the object surface. The results in Table 1 follow the above arrangement, keeping poses within the 90th percentile with respect to their ADD error and computing for these the ADD as well as the absolute angular and positional error statistics.

Figure 11 illustrates an indicative comparison of inference times for two different GPU models (specifically the GeForce RTX 3060 & RTX 3070) employed with two sequences for the 720×540 image resolution. These tests aim to quantify the impact the selection of an affordable GPU has on inference times. The RTX 3060 is equipped with 12GB of GDDR6 memory, which is considerably larger compared to the 8GB memory offered by the RTX 3070. However, since inferencing is a compute-bound operation and the RTX 3070 has a higher number of CUDA cores (5888) compared to those in the RTX 3060 (3584 cores), it achieves shorter processing times.

Overall, these findings attest that the proposed methodology can support the initialization or the re-initialization of our model-based tracker (Lourakis and Pateraki, 2021) with an approximate pose of reasonable accuracy. The tracker can thus be augmented by the presented pose estimator running in a parallel thread and providing an additional cue for pose estimation when necessary. On the other hand, the estimator is not fast enough for tracking-by-detection (Lepetit and Fua, 2005) in real-time.

6 CONCLUSION

Capitalizing on recent developments in object detection and localization, this paper has presented a methodology for spreader 6D pose estimation from a single image. It starts by constructing a photo-realistic textured mesh model of the spreader which is subsequently systematically rendered from different camera viewpoints to generate a training dataset augmented with the employed poses. Pose inference with EPOS (Hodaň et al., 2020a) yields a pose esti-

Table 1: Quantitative results for each test sequence and corresponding image sizes. The minimum, maximum and mean values are shown for ADD, absolute angular and positional errors.

Sequence	#frames	ADD error (m)			Absolute Angular Error (°)			Absolute Positional Error (m)		
		min	mean	max	min	mean	max	min	mean	max
0621_144051	538	0.012	0.131	0.359	0.11	1.81	5.79	0.028	0.309	1.917
0621_143959	581	0.015	0.109	0.230	0.06	1.50	4.57	0.008	0.273	1.256
090531	692	0.026	0.284	0.613	0.42	3.65	10.48	0.036	0.570	3.873
0621_124449	1300	0.012	0.284	0.949	0.25	4.66	19.15	0.017	0.934	4.761
083611	1060	0.029	0.230	0.642	0.17	4.35	11.77	0.034	0.535	3.525
081824	1336	0.016	0.194	0.563	0.11	1.87	6.65	0.018	0.641	3.028
091956	804	0.037	0.257	0.700	0.15	3.36	10.74	0.025	0.650	3.116
095324	695	0.08	0.686	1.286	0.47	7.93	16.36	0.029	0.905	2.389

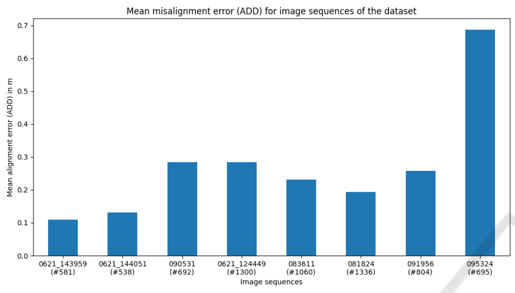

Figure 9: Mean misalignment error (ADD) for all eight image sequences. In the horizontal axis, the names of the sequences from the dataset are shown along with their corresponding #number of frames in parentheses. The vertical axis shows the mean ADD in meters (m).

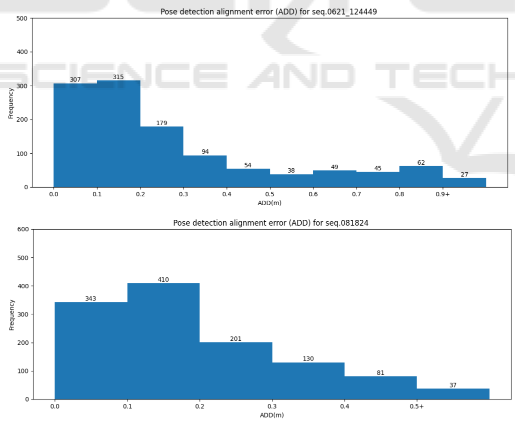

Figure 10: Distribution of the misalignment error (ADD) for two indicative image sequences, specifically image sequence 0621_12449 with 1300 frames (top) and sequence 81824 with 1336 frames (bottom).

mate that can complement recursive 3D tracking approaches such as (Lourakis and Pateraki, 2021) for bootstrapping and re-initialization. Comprehensive experiments performed with real-world images annotated with spreader poses have demonstrated the efficacy of the approach.

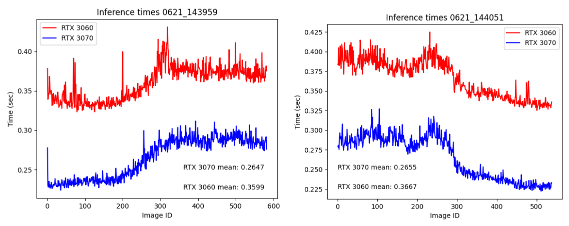

Figure 11: Inference times per image frame for two sequences using two different GPUs. Timings from sequence 0621_143959 (left) and sequence 0621_144051 (right) are shown. For both sequences, images of 720×540 pixels were used.

ACKNOWLEDGEMENTS

This work has received funding from the EU Horizon 2020 programme under GA No. 101017151 FELICE.

REFERENCES

Barath, D. and Matas, J. (2018). Graph-cut RANSAC. In *Proceedings of the IEEE conference on computer vision and pattern recognition*, pages 6733–6741.

Brachmann, E., Krull, A., Michel, F., Gumhold, S., Shotton, J., and Rother, C. (2014). Learning 6D object pose estimation using 3D object coordinates. In *European conference on computer vision*, pages 536–551. Springer.

Chen, L.-C., Zhu, Y., Papandreou, G., Schroff, F., and Adam, H. (2018). Encoder-decoder with atrous separable convolution for semantic image segmentation. In *Proceedings of the European conference on computer vision (ECCV)*, pages 801–818.

Drost, B., Ulrich, M., Bergmann, P., Hartinger, P., and Steger, C. (2017). Introducing MVTec ITODD – A dataset for 3D object recognition in industry. In *Proceedings of the IEEE international conference on computer vision workshops*, pages 2200–2208.

Fischler, M. and Bolles, R. (1981). Random sample consensus: A paradigm for model fitting with applications to image analysis and automated cartography. *Commun. ACM*, 24(6):381–395.

Garrido-Jurado, S., Muñoz Salinas, R., Madrid-Cuevas, F., and Marín-Jiménez, M. (2014). Automatic generation and detection of highly reliable fiducial markers under occlusion. *Pattern Recognition*, 47(6):2280–2292.

He, K., Gkioxari, G., Dollár, P., and Girshick, R. (2017). Mask R-CNN. In *IEEE International Conference on Computer Vision (ICCV)*, pages 2980–2988.

He, Y., Huang, H., Fan, H., Chen, Q., and Sun, J. (2021a). FFB6D: A full flow bidirectional fusion network for 6D pose estimation. In *Proceedings of the IEEE/CVF Conference on Computer Vision and Pattern Recognition*, pages 3003–3013.

He, Z., Feng, W., Zhao, X., and Lv, Y. (2021b). 6D pose estimation of objects: Recent technologies and challenges. *Applied Sciences*, 11(1):228.

Hinterstoisser, S., Lepetit, V., Ilic, S., Holzer, S., Bradski, G., Konolige, K., and Navab, N. (2012). Model based training, detection and pose estimation of texture-less 3D objects in heavily cluttered scenes. In *Asian Conf. on Computer Vision*, pages 548–562. Springer.

Hodaň, T., Baráth, D., and Matas, J. (2020a). EPOS: Estimating 6D pose of objects with symmetries. *IEEE Conference on Computer Vision and Pattern Recognition (CVPR)*.

Hodan, T., Haluza, P., Obdržálek, Š., Matas, J., Lourakis, M., and Zabulis, X. (2017). T-LESS: An RGB-D dataset for 6D pose estimation of texture-less objects. In *2017 IEEE Winter Conference on Applications of Computer Vision (WACV)*, pages 880–888. IEEE.

Hodaň, T., Sundermeyer, M., Drost, B., Labbé, Y., Brachmann, E., Michel, F., Rother, C., and Matas, J. (2020b). BOP challenge 2020 on 6D object localization. In *European Conference on Computer Vision*, pages 577–594. Springer.

Hu, H., Zhu, M., Li, M., and Chan, K.-L. (2022). Deep learning-based monocular 3D object detection with refinement of depth information. *Sensors*, 22(7).

Huynh, D. Q. (2009). Metrics for 3D rotations: Comparison and analysis. *J. Math. Imaging Vis.*, 35(2):155–164.

Jiang, X., Li, D., Chen, H., Zheng, Y., Zhao, R., and Wu, L. (2022). Uni6D: A unified CNN framework without projection breakdown for 6D pose estimation. In *Proceedings of the IEEE/CVF Conference on Computer Vision and Pattern Recognition*, pages 11174–11184.

Kim, S.-h. and Hwang, Y. (2021). A survey on deep learning based methods and datasets for monocular 3D object detection. *Electronics*, 10(4):517.

Kneip, L., Scaramuzza, D., and Siegwart, R. (2011). A novel parametrization of the perspective-three-point problem for a direct computation of absolute camera position and orientation. In *CVPR 2011*, pages 2969–2976. IEEE.

Labbe, Y., Carpentier, J., Aubry, M., and Sivic, J. (2020). CosyPose: Consistent multi-view multi-object 6D pose estimation. In *Proceedings of the European Conference on Computer Vision (ECCV)*.

Lepetit, V. and Fua, P. (2005). Monocular model-based 3D tracking of rigid objects: A survey. *Foundations and Trends in Computer Graphics and Vision*, 1(1).

Lepetit, V., Moreno-Noguer, F., and Fua, P. (2009). EPnP: An accurate O(n) solution to the PnP problem. *International journal of computer vision*, 81(2):155.

Lourakis, M. (2004). levmar: Levenberg-Marquardt nonlinear least squares algorithms in C/C++. [web page] http://www.ics.forth.gr/~lourakis/levmar/.

Lourakis, M. and Pateraki, M. (2021). Markerless visual tracking of a container crane spreader. In *IEEE/CVF International Conference on Computer Vision Workshops (ICCVW)*, pages 2579–2586.

Lourakis, M. and Pateraki, M. (2022a). Computer vision for increasing safety in container handling operations. In *Human Factors and Systems Interaction, International Conference on Applied Human Factors and Ergonomics (AHFE)*, volume 52.

Lourakis, M. and Pateraki, M. (2022b). Container spreader pose tracking dataset. Zenodo, https://doi.org/10.5281/zenodo.7043890.

Lourakis, M., Pateraki, M., Karolos, I.-A., Pikridas, C., and Patias, P. (2020). Pose estimation of a moving camera with low-cost, multi-GNSS devices. *Int. Arch. Photogramm. Remote Sens. Spatial Inf. Sci.*, XLIII-B2-2020:55–62.

Marchand, E., Uchiyama, H., and Spindler, F. (2016). Pose estimation for augmented reality: A hands-on survey. *IEEE Transactions on Visualization and Computer Graphics*, 22(12):2633–2651.

Ngo, Q. H. and Hong, K.-S. (2012). Sliding-Mode Antisway Control of an Offshore Container Crane. *IEEE/ASME Transactions on Mechatronics*, 17(2):201–209.

Rahman, M. M., Tan, Y., Xue, J., and Lu, K. (2019). Recent advances in 3D object detection in the era of deep neural networks: A survey. *IEEE Transactions on Image Processing*, 29:2947–2962.

Sahin, C. and Kim, T.-K. (2018). Recovering 6D object pose: a review and multi-modal analysis. In *Proceedings of the European Conference on Computer Vision (ECCV) Workshops*, pages 0–0.

Sun, J., Wang, Z., Zhang, S., He, X., Zhao, H., Zhang, G., and Zhou, X. (2022). OnePose: One-shot object pose estimation without CAD models. In *IEEE/CVF Conference on Computer Vision and Pattern Recognition (CVPR)*, pages 6815–6824.

van Ham, H., van Ham, J., and Rijsenbrij, J. (2012). *Development of Containerization: Success Through Vision, Drive and Technology*. IOS Press.

Wang, B., Zhong, F., and Qin, X. (2019). Robust edge-based 3D object tracking with direction-based pose validation. *Multimedia Tools and Applications*, 78(9):12307–12331.

Wang, G., Manhardt, F., Shao, J., Ji, X., Navab, N., and Tombari, F. (2020). Self6D: Self-supervised monocular 6D object pose estimation. In *European Conference on Computer Vision (ECCV)*, pages 108–125, Cham. Springer International Publishing.

Wu, Y., Kirillov, A., Massa, F., Lo, W.-Y., and Girshick, R. (2019). Detectron2. https://github.com/facebookresearch/detectron2.